JACS
JOURNAL OF THE AMERICAN CHEMICAL SOCIETY

Article

pubs.acs.org/JACS

Covalently Linked Dimer of Mn_3 Single-Molecule Magnets and Retention of Its Structure and Quantum Properties in Solution

Tu N. Nguyen,[†] Muhandis Shiddiq,[‡] Tuhin Ghosh,[†] Khalil A. Abboud,[†] Stephen Hill,[‡] and George Christou*,[†]

[†]Department of Chemistry, University of Florida, Gainesville, Florida 32611, United States,

[‡]National High Magnetic Field Laboratory and Department of Physics, Florida State University, Tallahassee, Florida 32310, United States

Supporting Information

ABSTRACT: $[Mn_3O(O_2CMe)_3(dpd)_{3/2})]_2(I_3)_2$ has been obtained from the reaction of 1,3-di(pyridin-2-yl)propane-1,3-dione dioxime ($dpdH_2$) with triangular $[Mn^{III}_3O(O_2CMe)(py)_3](ClO_4)$. It comprises two $[Mn^{III}_3O]^{7+}$ triangular units linked covalently by three dioximate ligands into a $[Mn_3]_2$ dimer. Solid state dc and ac magnetic susceptibility measurements reveal that each Mn_3 subunit of the dimer is a separate single-molecule magnet (SMM) with an $S = 6$ ground state and that the two SMM units are very weakly ferromagnetically exchange coupled. High-frequency EPR spectroscopy on a single crystal displays signal splittings indicative of quantum superposition/entanglement of the two SMMs, and parallel studies on MeCN/toluene (1:1) frozen solutions reveal the same spectral features. The dimer thus retains its structure and inter-Mn_3 coupling upon dissolution. This work establishes that covalently linked molecular oligomers of exchange-coupled SMMs can be prepared that retain their oligomeric nature and attendant inter-SMM quantum mechanical coupling in solution, providing a second phase for their study and demonstrating the feasibility of using solution methods for their deposition on surfaces and related substrates for study.

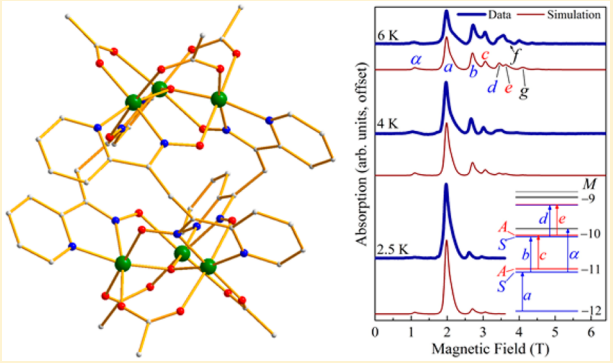

INTRODUCTION

Single-molecule magnets (SMMs) are molecules that function as nanoscale magnetic particles below their blocking temperature, T_B,[1−4] as a result of their significant magnetic moment and easy-axis magnetoanisotropy that lead to a large (vs kT) barrier to magnetization relaxation. They bring to nanomagnetism the advantages of molecular chemistry (ambient-temperature synthesis, solubility, crystallinity, monodispersity, organic ligands, etc.), and these have been crucial in demonstrating that SMMs also display fascinating quantum phenomena such as quantum tunneling of magnetization (QTM),[5,6] quantum phase interference,[7−9] spin−spin cross relaxation,[10] and quantum entanglement.[11−13] SMMs have consequently been proposed as qubits for quantum information processing[14−17] and as components in molecular spintronics devices.[18,19] These potential applications of SMMs require the quantum mechanical coupling of two or more SMMs to each other or to other components of a device while maintaining the intrinsic single-molecule properties of each SMM. Such couplings were successfully identified for hydrogen-bonded supramolecular pairs of $S = 9/2$ $[Mn_4O_3Cl_4(O_2CEt)_3(py)_3]$ SMMs and manifested as exchange-biased QTM, quantum superposition states, and quantum entanglement of SMMs.[11−13,20] However, reliance on hydrogen bonding to provide the inter-SMM interactions was a weakness of the previous work, since it is not so easy to control the oligomerization or guarantee retention of the oligomeric structure in solution. We therefore recently extended this work to aggregates of Mn SMMs linked by covalent organic linkages to provide greater control of various aspects of the oligomerization while still targeting molecular oligomers rather than polymers. We recently reported a $[Mn_3]_4$ tetramer of SMMs, covalently linked with dioximate linker groups,[21] as the first result of this new direction. It provided proof-of-feasibility for our chosen approach and for developing molecular multiqubit systems based on SMMs in which the quantum-mechanically coupled aggregates might be stable to dissociation in solution and thus provide a route for deposition of aggregates on surfaces without complications from fragmentation or other loss of structural integrity on dissolution, the problems almost always associated with hydrogen-bonded supramolecules,[20,22] or hydrogen-bonded or covalently linked 0-, 1-, 2-, or 3-D aggregates.[23−37] The methodology also provides a convenient means via ligand design to tune the strength (and ferro- or antiferromagnetic nature) of the inter-SMM coupling, as has been reported, for example, in the coupling strength in a series of Cr_7Ni dimers by modifying the

Received: March 13, 2015
Published: June 1, 2015

DOI: 10.1021/jacs.5b02677
J. Am. Chem. Soc. 2015, 137, 7160−7168

aromatic linker.[38] Ferromagnetic coupling within dimeric or trimeric molecular aggregates is relatively rare but has sometimes been achieved in non-SMMs through a spin polarization mechanism even when the metal ions are well separated.[39−44] An additional challenge with SMM oligomers that we had to now also address was the desire to achieve parallel alignment of the easy axes of the constituent SMM units to allow application of an external field parallel to these axes and thus minimize the number of parameters that must be included in order to model the nebulous and fragile quantum properties that are a major driving force of the program.

We report here a covalently linked dimer of Mn_3 SMMs obtained using a specially designed dioximate linker that also ensures parallel easy axes and show that the dimer exhibits weak ferromagnetic inter-Mn_3 exchange coupling. High-frequency electron paramagnetic resonance (HF-EPR) studies on a single crystal establish that the dimer exhibits quantum mechanical coupling leading to quantum superposition states (entanglement) of the two SMMs. Further, we demonstrate for the first time that this situation persists upon dissolution, the superposition states being detected by HF-EPR spectroscopy on a frozen solution.

RESULTS AND DISCUSSION

Synthesis and X-ray Structure. The synthesis of a dioximate-linked dimer of Mn_3 SMMs is based on the previous observation that the mono-oxime mpkoH will react with non-SMM $[Mn_3O(O_2CMe)_6(py)_3](ClO_4)$ (**1**) to give $[Mn_3O(O_2CMe)_3(mpko)_3](ClO_4)$ (**2**), which has an $S = 6$ ground state and is an SMM.[45] The cation of **2** (Figure 1) has C_3 symmetry with the acetate and $mpko^-$ ligands on opposite sides of the Mn_3 plane. The tripodal arrangement of oximates suggested that their replacement with dioximates should give molecular oligomers rather than polymers. This was confirmed with dioxime $pdpdH_2$ (Figure 1), which gave a rectangular $[Mn_3]_4$ tetramer,[21] but the conformationally flexible $pdpd^{2-}$ linkers were not "preprogrammed" to produce a particular structural topology, and neither were the Mn_3 planes parallel.

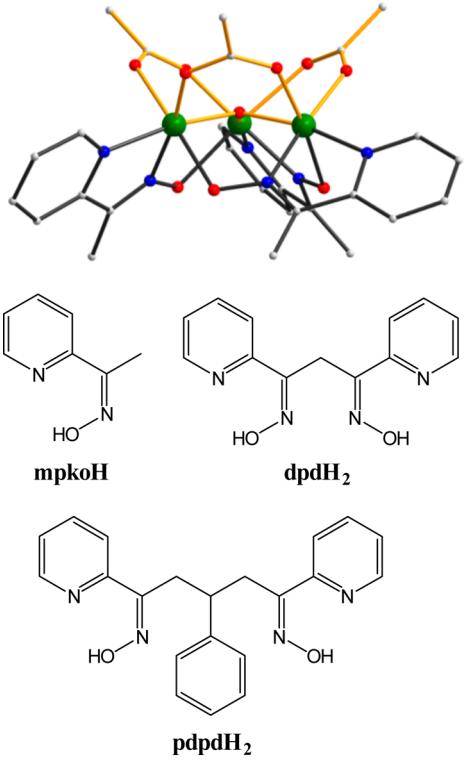

Figure 1. (Top) Cation of monomer **2** viewed along the Mn_3 plane showing the tripodal arrangements of the three acetate and three $mpko^-$ groups. Color code: Mn, green; N, blue; O, red; C, gray. (Bottom) Structures of the three dioximes mpkoH, $dpdH_2$, and $pdpdH_2$ mentioned in the text.

With proof-of-feasibility of the oligomerization strategy established, the first targeted oligomer was now a $[Mn_3]_2$ dimer with the two Mn_3 planes parallel to facilitate subsequent study of the quantum properties. Consideration of basic principles from the supramolecular chemistry field[46] led to selection of dioxime $dpdH_2$ (Figure 1), a fusion of two mpkoH units at the Me group. The single sp^3 carbon atom at the center reduces the conformational flexibility, and according to the directional bonding approach for constructing supramolecules,[46] the combination of a ∼109° ditopic dioximate with a tritopic Mn_3 unit should yield a $[Mn_3]_2$ dimer with three linker groups and parallel Mn_3 planes. Moreover, the firm binding by tridentate pyridyloximate groups of three dpd^{2-} linkers was considered favorable for imparting rigidity and robustness to the resulting dimer, hopefully leading to retention of the structure in solution. Also important in the selection of $dpdH_2$ was that a single sp^3 carbon atom was expected to ensure that the superexchange interaction between two Mn_3 SMMs would be very weak (but nonzero) and thus merely a small perturbation on a two-SMM system. We found no previous use of $dpdH_2$ in inorganic chemistry.

The $dpdH_2$ was synthesized using reported procedures for the dione and conversion to the dioxime.[47] Reaction of **1** with $dpdH_2$ and I_2 in a 2:3:6 molar ratio in CH_2Cl_2/EtOH (25:1 v/v) gave a dark brown solution, which was filtered, and the filtrate was allowed to slowly concentrate by evaporation to give black crystals of $[Mn_6O_2(O_2CMe)_6(dpd)_3)](I_3)_2$ (**3**) (eq 1). I_2 was added to prevent reduction of some of the Mn^{III} to Mn^{II}, as sometimes seen during preliminary studies of oligomerization of triangular Mn^{III}_3 complexes.

$$2[Mn_3O(O_2CMe)_6(py)_3]^+ + 3dpdH_2 \rightarrow [Mn_6O_2(O_2CMe)_6(dpd)_3]^{2+} + 6MeCO_2H + 6py \quad (1)$$

Complex **3** crystallizes in trigonal space group $P\bar{3}1c$ with the cation on a crystallographic C_3 axis. As targeted by the choice of $dpdH_2$, the structure of the Mn_6^{2+} cation consists of two $[Mn_3(\mu_3\text{-}O)]^{7+}$ units linked by three dpd^{2-} groups to give a $[Mn_3]_2$ dimer of crystallographic D_3 symmetry (Figure 2). The two Mn_3 planes are thus parallel. Each Mn_3 unit is an equilateral triangle (Table 1) and structurally very similar to that of monomer **2**, comprising a $[Mn_3(\mu_3\text{-}O)]^{7+}$ triangular unit whose edges are each bridged by one acetate and one pyridyloximate group and with the $\mu_3\text{-}O^{2-}$ ions lying slightly (∼0.29 Å) above their Mn_3 plane. The Mn^{III} oxidation states were confirmed by bond valence sum (BVS) calculations (Table S1, Supporting Information),[48] and their Jahn−Teller elongation axes (green bonds in Figure 2, right) are clearly along the O(carb)−Mn−O(ox) bonds (Table 1) and aligned in a propeller fashion, again as in **2**. Inspection of the crystal packing shows that not only are the two Mn_3 planes of each dimer parallel but also all dimer molecules are oriented identically (Figure S1, Supporting Information). There are no close interdimer contacts between carboxylate groups, with the

DOI: 10.1021/jacs.5b02677
J. Am. Chem. Soc. 2015, 137, 7160−7168

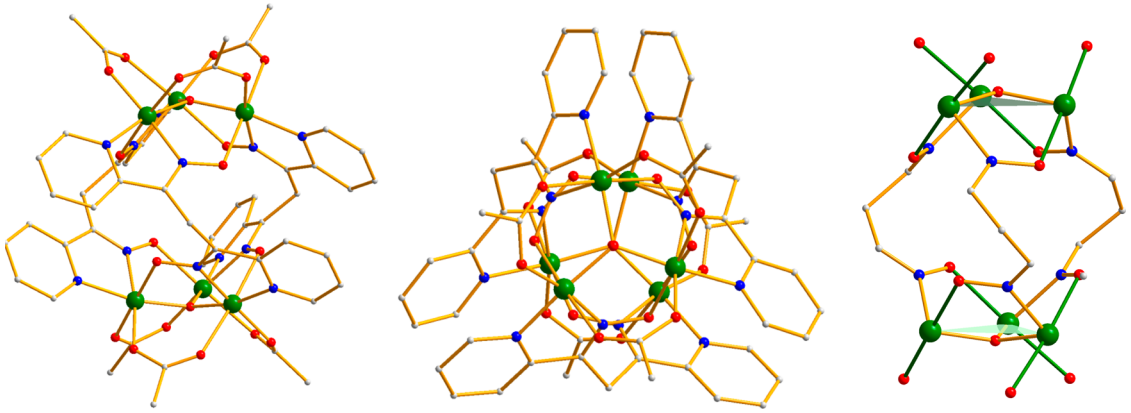

Figure 2. Cation of $[Mn_3]_2$ dimer **3** viewed almost along a C_2 symmetry axis (left) and along the C_3 axis (middle). Also shown (right) is the connectivity depicting the Mn_3 planes and the propeller arrangement of the Jahn–Teller axes, shown as green bonds. Color code: Mn, green; N, blue; O, red; C, gray. Hydrogen atoms have been omitted for clarity.

Table 1. Selected Mn_3 Core Distances and Angles for 3

parameter[a]	value (Angstroms or degrees)[b]
Mn···Mn	3.2005(7)
Mn1–O^{2-}	1.8704(6)
Mn1–O(carb)	1.935(2)
Mn1–O(carb)	2.200(2)
Mn1–N(ox)	2.012(2)
Mn1–O(ox)	2.167(2)
Mn1–N(py)	2.033(2)
Mn–O^{2-}–Mn	117.64(5)
O^{2-}-to-Mn_3 plane	0.29
Mn–N–O–Mn[c]	3.134(4)

[a]carb = carboxylate, ox = oximate, py = pyridyl. [b]Crystallographic C_3 symmetry. [c]Mn–oximate–Mn torsion angle.

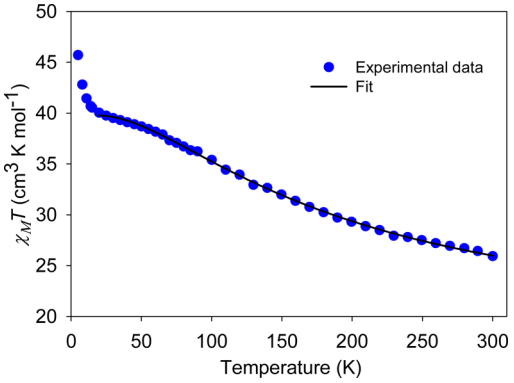

Figure 3. $\chi_M T$ per dimer vs T plot for **3** in a 0.1 T dc field. Solid line is the fit of the 20–300 K data, as described in the text. See text for fit parameters.

shortest separation being ~3.7 Å (Figure S2, Supporting Information, top). Also, the shortest distance between Mn ions of adjacent dimers is ~8.16 Å, suggesting that dipolar interactions between different $[Mn_3]_2$ dimers can be neglected. This is consistent with the absence of an exchange bias in the magnetization hysteresis loops for monomer **2**, where the separations between adjacent Mn_3 molecules are comparable to those between adjacent dimers in **3**.[45] This will be important to the magnetic and EPR discussions below.

Magnetic Studies. Two important questions needing to be addressed by the magnetic studies on **3** were (i) is each Mn_3 subunit still an SMM with $S = 6$ and (ii) is there any evidence for a weak inter-Mn_3 interaction within the $[Mn_3]_2$ dimer? Variable-temperature, direct current (dc) magnetic susceptibility (χ_M) measurements were performed on dried samples of **3**, restrained in eicosane to prevent torquing, in an applied field of 1.0 kG (0.10 T) and in the 5.0–300 K range. $\chi_M T$ per dimer increases steadily from 25.93 cm^3 K mol^{-1} at 300 K to a quasi-plateau value of 40.04 cm^3 K mol^{-1} at 20 K and then increases steeply to 45.70 cm^3 K mol^{-1} at 5.0 K (Figure 3). The profile above 20 K is the same as that for monomer **2** and is as expected for ferromagnetic coupling within each Mn_3 unit giving an $S = 6$ ground state. The quasi-plateau value at low T is as expected for two ostensibly noninteracting $S = 6$ units with g slightly <2.0, which is typical for Mn^{III}; the spin-only ($g = 2.0$) value for $S = 6$ is 21 cm^3 K mol^{-1} and thus 42 cm^3 K mol^{-1} for a dimer of noninteracting $S = 6$ units. The increase in $\chi_M T$ at T < 20 K is assigned to very weak ferromagnetic coupling between the two $S = 6$ Mn_3 units, and thus, at extremely low T it would be expected to approach the value for an $S = 12$ ground state ($\chi_M T = 78$ cm^3 K mol^{-1} for $g = 2.0$). The data thus indicate that each Mn_3 unit does indeed still possess an $S = 6$ ground state (as does monomer **2**) and that there is a weak ferromagnetic inter-Mn_3 interaction.

Attempts to fit the 20–300 K data to an equilateral triangle model were unsatisfactory (Figure S3, Supporting Information), assignable to the crystallographic symmetry masking small local distortions from equilateral symmetry; the latter were seen for **2** and related monomers that had no crystallographic symmetry.[45] The 20–300 K data were thus fit to the theoretical $\chi_M T$ vs T expression for a dimer of Mn^{III}_3 isosceles triangles, assuming the two Mn_3 units are non-interacting.[48] A similar treatment of magnetic data was performed for a $[Cu_2]_2$ dimeric molecule reported previously.[49] The Heisenberg–Dirac–Van Vleck (HDVV) spin Hamiltonian is given in eq 2, which can be converted into the equivalent form in eq 3

$$\hat{H} = -2J(\hat{S}_1\cdot\hat{S}_2 + \hat{S}_1\cdot\hat{S}_{2'}) - 2J'\hat{S}_2\cdot\hat{S}_{2'} \quad (2)$$

$$\hat{H} = -J(\hat{S}_T^{\,2} - \hat{S}_A^{\,2} - \hat{S}_1^{\,2}) - J'(\hat{S}_A^{\,2} - \hat{S}_2^{\,2} - \hat{S}_{2'}^{\,2}) \quad (3)$$

using the substitutions $\hat{S}_A = \hat{S}_2 + \hat{S}_{2'}$ and $\hat{S}_T = \hat{S}_A + \hat{S}_1$; S_T is the total spin of the unit, taking values of $S_T = 0$–6 since $S_1 = S_2 = S_{2'} = 2$. The eigenvalues of eq 3 are given by eq 4.

DOI: 10.1021/jacs.5b02677
J. Am. Chem. Soc. 2015, 137, 7160–7168

$$E(S_T, S_A) = -J[S_T(S_T + 1) - S_A(S_A + 1)] - J'[S_A(S_A + 1)] \quad (4)$$

The fit (solid line in Figure 3) gave J = +6.8(1) cm^{-1}, J' = +26.3(4) cm^{-1}, and g = 1.95(1), with temperature-independent paramagnetism (TIP) held constant at 600 × 10^{-6} cm^3 mol^{-1}. These values, including the TIP, are comparable to those for **2** and other Mn^{III}_3 triangular units.[45,50] The root-mean-square J vs J' error surface for the fit (Figure S4, Supporting Information) shows (i) a second local minimum of slightly lower quality with J = +20.4(1) cm^{-1}, J' = −0.8(4) cm^{-1}, and g = 1.95(1), corresponding to the second means of distorting an equilateral triangle to isosceles (as expected, the two minima are related, both with an average J_{av} of +13.3 cm^{-1}) and (ii) the $J = J'$ region between the two fit minima is a saddle point, supporting the poor fit of the data to an equilateral triangle model.

To confirm the ground state of each Mn_3 and to estimate the axial zero-field splitting parameter, D, magnetization (M) data were collected in the 1.8−10 K range in dc fields (H) up to 7 T and are plotted as $M/N\mu_B$ vs H/T in Figure 4 (N is Avogadro's

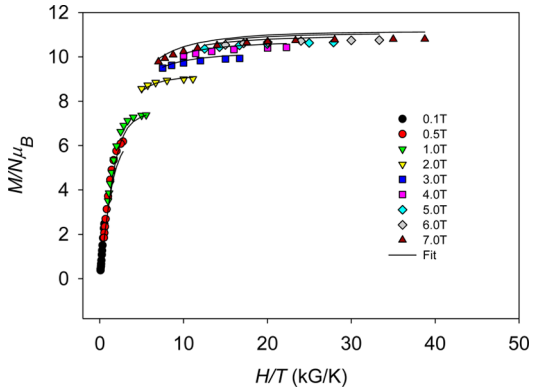

Figure 4. Magnetization (M) data per Mn_3 unit of **3** plotted as $M/N\mu_B$ vs H/T. Solid lines are the fit of the data; see text for fit procedure and obtained fit parameters.

constant, and μ_B is the Bohr magneton). Data in the 1−7 T range (lower fields were avoided to minimize interference from the very weak inter-Mn_3 interactions, see below) were fit by diagonalization of the spin Hamiltonian matrix assuming only the ground state is populated, incorporating uniaxial anisotropy ($D\hat{S}_z^2$) and Zeeman terms and employing a full powder average. The spin Hamiltonian is given by eq 5 ($\hat{S}_z$ is the easy-axis (z) spin projection, and μ_0 is the vacuum permeability).

$$\hat{H} = D\hat{S}_z^{\,2} + g\mu_B\mu_0\hat{S}\cdot H \quad (5)$$

The best fit (solid lines in Figure 4) gave S = 6, D = −0.24(1) cm^{-1}, and g = 1.89(1). The overall fit is good, but some discrepancies between the experimental data and the fit lines point to the influence of some effects not incorporated in eq 5, such as inter-Mn_3 interactions and the presence of rhombic anisotropy, E, the latter consistent with isosceles rather than equilateral Mn_3 units.

Alternating current (ac) susceptibility data on **3** in the 1.8−15 K range were collected using a 3.5 G ac field at frequencies up to 1500 Hz. The in-phase χ'_MT (Figure 5) is very similar to the dc χ_MT in the 5.0 ≤ T ≤ 15 K range: χ'_MT is 45.89 and 40.18 cm^3 K mol^{-1} at 5.0 and 15 K, respectively, essentially

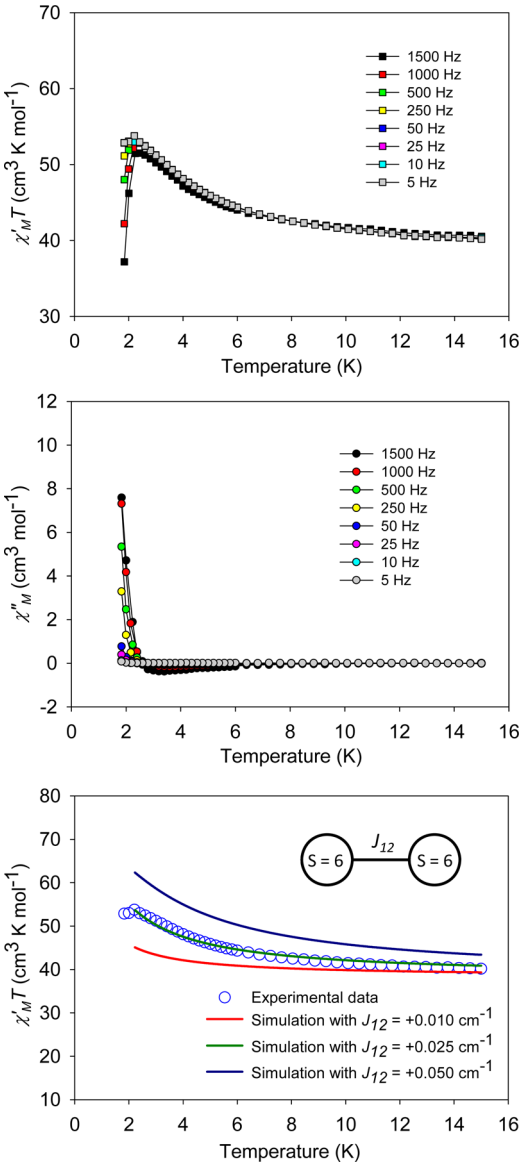

Figure 5. Alternating current susceptibility data for **3**: (top) in-phase χ'_MT vs T plot at the indicated frequencies; (middle) out-of-phase χ''_M vs T plot; and (bottom) MAGPACK simulation of the χ'_MT vs T data at 5 Hz ac frequency (excluding two lowest T points) as two S = 6 units with exchange interaction J_{12} of the indicated magnitudes. g was held constant at 1.91.

identical within experimental error to the χ_MT of 45.70 and 40.53 cm^3 K mol^{-1} at these temperatures. This indicates that the dc data is negligibly affected by Zeeman population problems from the 0.1 T field. Below 5.0 K, χ'_MT can be seen to continue increasing until ∼2 K, where frequency-dependent decreases appear due to slow magnetization relaxation of the Mn_3 SMM units. Concomitant with the latter are out-of-phase χ''_M signals (Figure 5). Since each Mn_3 unit is in its S = 6 ground state by ∼20 K, the 1.8−15 K data were simulated using the program MAGPACK,[51] to a model comprising two S = 6 units interacting with J_{12}. We used the ac χ'_MT data because of its greater T range and to preclude any effects of an applied dc field. The only variable in the simulation was J_{12}, and the obtained curves (Figure 5, bottom) indicate a very weak inter-Mn_3 coupling of J_{12} ≈ +0.025 cm^{-1}. The ac data thus confirm **3**

DOI: 10.1021/jacs.5b02677
J. Am. Chem. Soc. 2015, 137, 7160−7168

to be a dimer of $S = 6$ Mn_3 SMMs with a very weak inter-Mn_3 ferromagnetic interaction (J_{12}).

If there are weak interdimer antiferromagnetic interactions present, these would serve to decrease $\chi'_M T$ below 15 K. Thus, the observed increasing $\chi'_M T$ below 15 K would then be the net sum of an increase from intradimer ferromagnetic interactions and a decrease from antiferromagnetic ones between adjacent dimers. If this were the case, the obtained J_{12} from the simulation would be an underestimate of its true value. However, the EPR studies to be described below give a J_{12} value in excellent agreement with that from the $\chi'_M T$ simulation, indicating insignificant contributions to the $\chi'_M T$ below 15 K from effects other than the intradimer J_{12}.

We assign the ferromagnetic nature of the J_{12} coupling as arising from a spin polarization mechanism through the central sp^3 C atom, caused by spin density delocalized into the dpd^{2-} π systems from the Mn d_π magnetic orbitals (Figure 6). This will

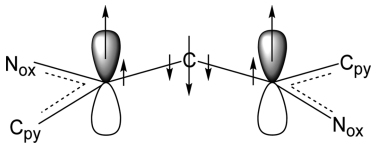

Figure 6. Proposed origin of the inter-Mn_3 ferromagnetic coupling by spin polarization of σ-bonding electrons to the central sp^3 C atom of the dpd^{2-} linker by the spin density in the orthogonal π system. N_{ox} = oximate N atom; C_{py} = 2-C atom of the pyridine ring.

dominate the direct σ-spin delocalization from the Mn d_σ (d_{z^2}) orbitals through the σ backbone, which would favor antiferromagnetic coupling but is expected to attenuate rapidly with the number of bonds.

The combined structural and magnetic data for **3** emphasize that this dimeric $[Mn_3]_2$ molecule is distinctly different from all other Mn_6 molecules reported in the literature that can be described as containing two Mn_3 triangular units.[52−56] **3** is a $[Mn_3]_2$ dimer of two very weakly coupled Mn_3 SMMs connected by a long dioximate linker, whereas the other Mn_6 molecules contain monatomic oxo bridges and thus much stronger couplings between their two halves, and they are therefore best described as Mn_6 monomers.

High-Frequency EPR (HF-EPR) Spectroscopy. HF-EPR studies were carried out on a single crystal of **3** to accurately determine the axial spin Hamiltonian parameters for each Mn_3 unit and the inter-Mn_3 exchange coupling strength, J_{12}. Measurements were then performed on a MeCN/toluene (1:1 v/v) solution of **3** to determine if the dimers remain intact in solution and, if so, to what extent any quantum mechanical coupling seen in the solid state between the two Mn_3 units is affected.

Assuming an $S = 6$ ground state and neglecting off-diagonal transverse anisotropy terms, the effective spin Hamiltonian (to fourth order) for an isolated/uncoupled Mn_3 SMM is given by eq 6 for a field applied parallel to its easy axis ($H \| z$);[57,58] the label i (= 1, 2) denotes the two Mn_3 units of the dimer

$$\hat{H}_i = D\hat{S}_{zi}^2 + B_4^0\hat{O}_{4,i}^0 + g_z\mu_B\mu_o H\hat{S}_{zi} \tag{6}$$

$D\hat{S}_{zi}^2$ represents the dominant second-order axial anisotropy, and $B_4^0\hat{O}_{4,i}^0$ characterizes a weaker (albeit significant) fourth-order axial anisotropy.[59] D, B_4^0, and g_z parametrize the three terms of eq 6 and are assumed identical for each half of the dimer. Omission of transverse anisotropy terms containing $\hat{S}_{xi}$ and $\hat{S}_{yi}$ does not affect the spectra, which are dominated by transitions between large $|m_i|$ states (m_i refers to the projection of S_i); such terms generate only the weak avoided level crossings that give rise to magnetic quantum tunneling.[58]

For two coupled Mn_3 SMMs, the effective dimer Hamiltonian ($\hat{H}_D$) is given by eq 7,[11] where the last term describes the exchange coupling within the dimer.

$$\hat{H}_D = \hat{H}_1 + \hat{H}_2 - 2J_{12}\hat{S}_1\cdot\hat{S}_2 \tag{7}$$

As reported elsewhere,[60] the dimer Hamiltonian matrix can be separated into the diagonal and off-diagonal terms given in eq 8, where $\hat{S}_i^{\pm}$ denote raising/lowering operators and

$$\begin{aligned}\hat{H}_D &= [\hat{H}_1 + \hat{H}_2 - 2J_z\hat{S}_{z1}\hat{S}_{z2}] + \{-J_{xy}(\hat{S}_1^+\hat{S}_2^- + \hat{S}_1^-\hat{S}_2^+)\} \\ &= \hat{H}_{0D} + \hat{H}'\end{aligned} \tag{8}$$

J_z and J_{xy} characterize the longitudinal and transverse exchange interaction strengths, respectively. The eigenvectors of $\hat{H}_{0D}$ may be expressed as products of the uncoupled eigenvectors, $|m_1\rangle$ and $|m_2\rangle$, associated with the individual halves of the dimer (the solutions to eq 6); these are abbreviated $|m_1,m_2\rangle$.

The EPR transitions associated with $\hat{H}_{0D}$ are simply those of the individual Mn_3 units, with small corrections that take into account the longitudinal exchange bias $[-2J_z m_1 m_2]$ between the two dimer halves. Previous simulations for a dimer of $S = 9/2$ Mn_4 SMMs in which only the easy-axis component $(-2J_z\hat{S}_{z1}\hat{S}_{z2})$ of the exchange interaction is operative show that the low-temperature HF-EPR spectrum is barely discernible from that of an isolated Mn_4 monomer, with more-or-less evenly spaced resonances and a fairly smooth peak-to-peak variation in intensity.[11] The spectrum is simple because any EPR transition involving one Mn_3 unit (subject only to a longitudinal bias from the other Mn_3) is degenerate with the same transition involving the other Mn_3 unit (subject to the same longitudinal bias), i.e., the eigenvalues of $\hat{H}_{0D}$ are invariant with respect to any permutation of the spin labels. However, the situation is different when the off-diagonal term in eq 8, $\hat{H}'$, is included. This interaction gives rise to a true quantum mechanical coupling of the two Mn_3 units so that EPR transitions can no longer be described as excitations of individual Mn_3 SMMs. $\hat{H}'$ mixes (entangles) the uncoupled product states, $|m_1,m_2\rangle$, in a manner that conserves the total angular momentum, $M = m_1 + m_2$, giving rise to eigenvectors that are either symmetric (S) or antisymmetric (A) superpositions of the original product states. The eigenvalues remain invariant to permutations of spin labels. However, the entanglement lifts all degeneracies that existed among uncoupled product states, e.g., the $M = -11$ states $|-6,-5\rangle$ and $|-5,-6\rangle$ (see inset to Figure 7). The outcome is a far more complex EPR spectrum, provided coherence is maintained among superposition states on EPR time scales (~ns).[60]

For the single-crystal HF-EPR measurements, the sample was first aligned in situ to have its easy axis parallel to the applied magnetic field ($H \| z$). The spectra in Figure 7 were recorded at 148.7 GHz for several temperatures, and the best simulations are included below each experimental trace. As noted above, the spectra are more complex than those for an isolated SMM, with uneven peak spacings and intensities indicating coherent coupling between the two Mn_3 units of the dimer. Indeed, the spectra bear no resemblance to either those obtained for isolated Mn_3 SMMs (equivalent to $J_{12} = 0$ in the present case)[45,61,62] or the well-known Mn_6 SMMs (equivalent to

DOI: 10.1021/jacs.5b02677
J. Am. Chem. Soc. 2015, 137, 7160−7168

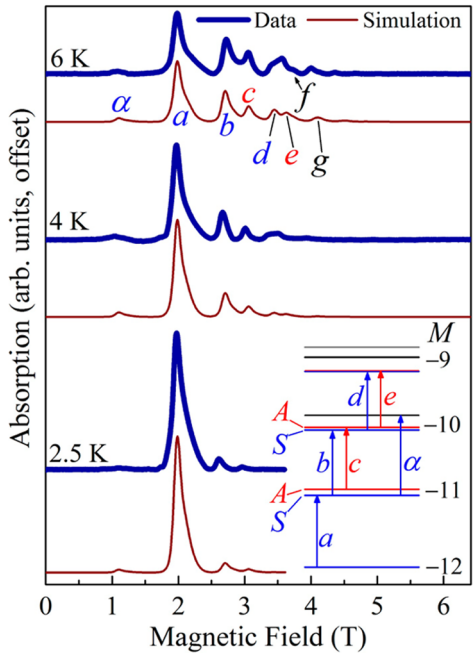

Figure 7. Temperature-dependent single-crystal HF-EPR absorption spectra for **3** at 148.7 GHz, with $H\|z$ and at the indicated temperatures. Simulations are included below each experimental trace (see text for further explanation). Some of the HF-EPR peaks are labeled according to transition assignments given in the inset and Figure S6, Supporting Information.[48] The inset represents the lowest 10 (out of 169 total) high-field eigenstates of the dimer, labeled according to their spin projection $M = m_1 + m_2$ and parity (symmetric (S) or even = blue; antisymmetric (A) or odd = red); vertical displacement represents energy ($M = -12$ is the ground state), while the horizontal axis has no significance. Several of the HF-EPR transitions labeled in the main figure are represented by vertical arrows in the inset.

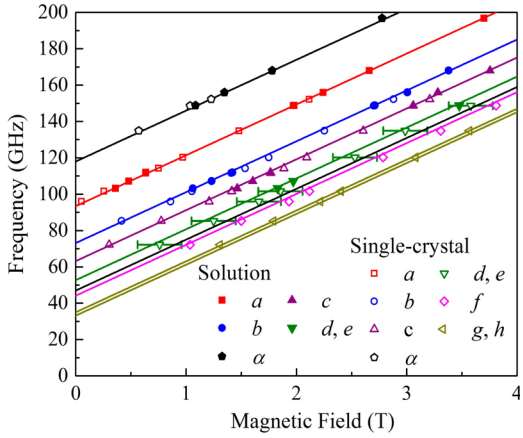

Figure 8. Compilation of peak positions and frequencies extracted from multifrequency (from ∼70 to 200 GHz) single-crystal and solution HF-EPR spectra such as those displayed in Figures 7 and 9. Each series of resonances (a, b, etc., see legend) lies on a straight line corresponding to the energy difference between pairs of eigenstates in Figure S6, Supporting Information. As can be seen, good agreement with theoretical expectations is achieved at all frequencies.

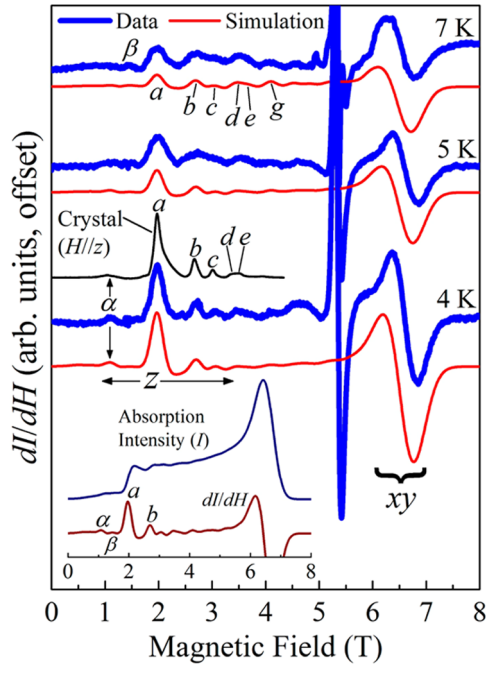

Figure 9. Solution HF-EPR spectra for **3** (10 mM in MeCN/toluene, 1:1 v/v) at 148.8 GHz and at the approximate temperatures indicated. Absorption (I) extends from the parallel ($H\|z$) to the perpendicular ($H\|xy$) components of the single-crystal spectrum (see lower inset and main text for further explanation). In the experimental derivative mode (dI/dH) spectra, the parallel and perpendicular components are separated by strong $g = 2.00$ signals close to 5.3 T (most likely due to isotropic impurity spins in the frozen glass and sample holder). Simulations are included below each experimental trace (see text for further explanation), and the 4 K single-crystal spectrum ($H\|z$) from Figure 7 is also included for further comparison; simulations do not reproduce the impurity signals. Some of the HF-EPR peaks have been labeled according to assignments given in Figures 7 and S6, Supporting Information.[48] (Inset) Simulated 4 K absorption spectrum along with the corresponding derivative (dI/dH).

strongly coupled Mn_3 triangles, i.e., $J_{12} > |D|$).[62,63] The strongest resonances have been labeled, with peak assignments given in the inset and in Figure S6, Supporting Information.[48] All transitions conserve parity, i.e., excitations only take place from S (A) states to S (A) states (see inset to Figure 7). The simulation parameters are $D = -0.22$ cm^{-1}, $B_4^0 = -7 \times 10^{-5}$ cm^{-1}, $g_z = 2.00$, and isotropic exchange $J_z = J_{xy} = J_{12} = +0.025$ cm^{-1}; an asymmetric distribution in D ($\sigma^+ = 0.004$ cm^{-1}, $\sigma^- = 0.02$ cm^{-1}) was included to reproduce the line shapes. The values of D and J_{12} are in excellent agreement with those deduced from the fits to low-temperature ac susceptibility and M vs H data, confirming the ferromagnetic coupling within the dimer. Overall, excellent agreement is achieved between the simulations and single-crystal HF-EPR measurements, not only in Figure 7 but also at many other frequencies in the 70−200 GHz range, as seen in Figure 8.

Temperature-dependent HF-EPR spectra recorded at 148.8 GHz in derivative mode (dI/dH; I is the absorption intensity) for a 10 mM solution of **3** are displayed in Figure 9; the data are noisier than those in Figure 7 due to the low spin concentration. Because the measurement is performed on molecules frozen into a glass, EPR absorption occurs for all possible molecular orientations. Hence, the spectrum spans from the lowest field transitions for a crystal (for which $H\|z$) to those at the highest field (for which $H\perp z$). dI/dH then gives a peak (or dip) at each point in the absorption spectrum corresponding to the onset of a new EPR transition (see lower inset to Figure 9);[64] thus, peaks occur for molecules with $H\|z$, while dips occur for molecules with $H\|xy$. In this way, one may

DOI: 10.1021/jacs.5b02677
J. Am. Chem. Soc. 2015, 137, 7160−7168

directly compare solution dI/dH spectra to those obtained in absorption mode for a single crystal (see 4 K data in Figure 7). Rigorous dI/dH simulations generated from orientation-averaged spectra are included below each experimental trace;[60] exactly the same Hamiltonian parameters were employed as those given above, with g_{xy} = 1.94. As can be seen in Figure 9, excellent agreement is obtained both between experiment and simulation and between the solution and the single-crystal spectra. The clear observation of peaks *b* and *c* at 4 K (as well as others such as α) provides strong confirmation that the dimers remain intact in solution and that they retain the entanglement observed in the solid state.

Although no clear rhombic E term could be detected from the HF-EPR measurements, it proved essential to include a significant strain in E (σ_E = 0.06 cm^{-1}, centered at E = 0)[65] in order to account for the lack of fine structure in the *xy* region of the solution spectrum (Figure 9). The orientations of the Mn^{III} Jahn−Teller axes can potentially project significant anisotropy into the *xy* plane,[45] but exact C_3 symmetry of the Mn_3 units would lead to a cancellation of the second-order transverse anisotropy (E).[57] Nevertheless, disorder (especially in a frozen solution) could account for an emergence of a significant distribution in E due to local deviations from C_3 symmetry.[57,58] The latter was also suggested to be occurring in the solid state to explain the fits of the variable-temperature susceptibility and magnetization data and the asymmetric distribution in D.[66]

CONCLUSIONS

A $[Mn_3]_2$ SMM dimer has been targeted and achieved employing covalent dpd^{2-} dioximate linkers. The triangular Mn_3 units are parallel, each has an S = 6 ground state from intra-Mn_3 ferromagnetic couplings, and the inter-Mn_3 interaction (J_{12}) is also ferromagnetic for the first time in SMM oligomers, but very weakly so. There is no evidence from any of the data for noticeable interactions (dipolar or superexchange) between adjacent dimers in the solid state, which is consistent with the absence of any significant interdimer contacts in the crystal structure and the large separations between Mn ions in adjacent dimers.

The J_{12} interaction quantum mechanically couples the two Mn_3 SMMs in each dimer, generating superposition states and entanglement that are manifested as splittings in the HF-EPR spectra. The same features at the same spectral positions are observed in a frozen solution, the first time that this quantum coupling of two separate SMMs has been detected in this phase. This spectral similarity suggests that the structure is quite robust and resists any significant deformation/distortion that might affect such a weak inter-Mn_3 coupling. In addition, the range of solvent environments that the dimer molecules experience due to the many C−H···N hydrogen bonds, $\pi-\pi$ stacking, and other interactions possible with polar MeCN and aromatic toluene solvent molecules similarly have no discernible effect on the strength of the inter-Mn_3 coupling. Thus, their study in solution opens up a new direction in coupled-SMM oligomers, and their robustness also offers a feasible means for their deposition on surfaces for device studies. Finally, studies in progress are targeting higher SMM oligomers with parallel easy axes, inter-SMM coupling, and robustness in solution.

EXPERIMENTAL SECTION

All manipulations were performed under aerobic conditions using chemicals and solvents as received unless otherwise stated. The dioxime $dpdH_2$ was synthesized following a reported procedure.[47]

Synthesis of $[Mn_6O_2(O_2CMe)_6(dpd)_3)](I_3)_2$ (3). Reaction of **1** (0.044 g, 0.050 mmol) with $dpdH_2$ (0.019 g, 0.075 mmol) and I_2 (0.038 g, 0.15 mmol) in CH_2Cl_2/EtOH (25 mL/1 mL) gave a dark brown solution. The I_2 was present to preclude reduction of some Mn^{III} to Mn^{II}, as seen in some preliminary studies of oligomerization of triangular Mn^{III}_3 complexes. The solution was filtered, and the filtrate was left to concentrate by slow evaporation at ambient temperature. Well-formed X-ray quality crystals of **3** slowly formed over a few days and were collected by filtration, washed with CH_2Cl_2/EtOH, and dried in vacuum; the yield was 0.025 g (~22% based on Mn). Anal. Calcd (Found) for **3** ($C_{51}H_{48}Mn_6N_{12}O_{20}I_6$) C, 27.35 (27.38); H, 2.16 (1.89); N, 7.50 (6.96); I, 33.99 (34.34). The I_3^- anions were badly disordered, and the stoichiometry of two I_3^- per Mn_6^{2+} cation was confirmed by the iodine analysis. Selected IR data (KBr disk, cm^{-1}): 1601 (s), 1570 (s), 1521 (m) 1473 (s), 1384 (vs), 1332 (s), 1186 (s), 1159 (m), 1110 (s), 1063 (w), 1046(w), 1032 (w), 934 (w), 770 (m), 742 (w), 698 (m), 658(m), 608 (m), 563 (w).

X-ray Crystallography. X-ray Intensity data were collected at 100 K on a Bruker DUO diffractometer using Mo Kα radiation (λ = 0.71073 Å) and an APEXII CCD area detector. The sample for crystallography was maintained in mother liquor to prevent crystal degradation. A suitable crystal of **3** was attached to a glass fiber using silicone grease and transferred to a goniostat where it was cooled to 100 K for data collection. Raw data frames were read by the program SAINT and integrated using 3D profiling algorithms. The resulting data were reduced to produce *hkl* reflections, their intensities, and estimated standard deviations. The data were corrected for Lorentz and polarization effects, and numerical absorption corrections were applied based on indexed and measured faces. The structures were solved and refined in SHELXTL6.1[67] using full-matrix least-squares refinement. The non-H atoms were refined with anisotropic thermal parameters, and all of the H atoms were calculated in idealized positions and refined riding on their parent atoms. Final cell data and refinement indices are collected in Table 2.

Table 2. Crystal Data and Structure Refinement Parameters for Complex 3

formula	$C_{51}H_{48}I_6Mn_6N_{12}O_{20}$
fw, g mol^{-1}	2240.05
space group	$P\bar{3}$ 1*c*
a, Å	16.5692(10)
b, Å	16.5692(10)
c, Å	18.2847(11)
α, deg	90
β, deg	90
γ, deg	120
V, Å^3	4347.3(6)
Z	2
T, K	100(2)
radiation, Å	0.71073
ρ_{calcd}, g cm^{-3}	1.711
μ, mm^{-1}	3.036
R_1 [$I > 2\sigma(I)$]	0.0496
wR_2 (F^2, all data)	0.1383

The asymmetric unit consists of a 1/6 Mn_6^{2+} cluster and two 1/6 I_3^- counterions located on $\bar{3}$ symmetry elements. The I_3^- ions were heavily disordered and could not be modeled properly; thus, the program SQUEEZE,[68] a part of the PLATON package of crystallographic software,[69] was used to calculate the disorder area and remove its contribution to the overall intensity data.

DOI: 10.1021/jacs.5b02677
J. Am. Chem. Soc. 2015, 137, 7160−7168

High-Frequency EPR (HF-EPR) Spectroscopy. HF-EPR spectra were collected at the Electron Magnetic Resonance facility of the U.S. National High Magnetic Field Laboratory. Oriented single-crystal measurements were performed using a high-sensitivity cavity perturbation technique that additionally permits two-axis sample rotation relative to the applied magnetic field direction.[70] A vector network analyzer was employed as a tunable microwave source and phase-sensitive detector, enabling measurements over a wide frequency range spanning from the fundamental TE_{011} mode (51 GHz with a quality factor Q = 20 000) of the cylindrical cavity to frequencies in excess of 200 GHz, corresponding to higher-order modes of the cavity.[70,71] In order to avoid sample degradation due to solvent loss, wet single crystals were coated with paratone-N oil immediately after removal from their mother liquor and then cooled initially under 1 atm of He gas. Single-crystal spectra were recorded in absorption mode. Angle-dependent measurements (not shown) were initially carried out in order to align (to within 5°) the magnetic field with the magnetic easy (z) axis of the crystal. For solution samples, spectra were collected using a broad band (10−700 GHz) transmission probe in which microwaves are propagated in to and out of a 17 T superconducting magnet through cylindrical light pipes.[72] Tunable microwave radiation was generated using a phase-locked Virginia Diodes solid-state source operating at 13 ± 1 GHz, followed by a chain of solid-state multipliers and amplifiers. Field modulation was employed in conjunction with a phase-sensitive homodyne detection scheme using a cold bolometer, yielding derivative mode (dI/dH) spectra. Temperature control was achieved in both experiments using He gas flow cryostats. While the temperature of the single-crystal sample was well calibrated, there is a significant uncertainty (±1 K) in the temperature of the frozen solution sample. Spectral simulations were performed using the program EasySpin.[59]

Other Measurements. Infrared spectra were recorded in the solid state (KBr pellets) on a Nicolet Nexus 670 FTIR spectrometer in the 400−4000 cm^{-1} range. Elemental analyses (C, H, and N) were performed by the in-house facilities of the University of Florida, Chemistry Department. UV−vis spectra were obtained on a Jasco V570 spectrometer in the 200−800 nm. Variable-temperature direct current (dc) and alternating current (ac) magnetic susceptibility data were collected using a Quantum Design MPMS-XL SQUID magnetometer equipped with a 7 T magnet and operating in the 1.8−300 K range. Samples were embedded in solid eicosane to prevent torquing. Magnetization vs field and temperature data were fit using the program MAGNET.[73] Pascal's constants were used to estimate the diamagnetic correction, which was subtracted from the experimental susceptibility to give the molar paramagnetic susceptibility (χ_M).

■ ASSOCIATED CONTENT

Ⓢ Supporting Information

BVS calculation data, Van Vleck equation, fit of dc susceptibility vs T data, fit error surface, and additional structural and EPR figures. The Supporting Information is available free of charge on the ACS Publications website at DOI: 10.1021/jacs.5b02677.

■ AUTHOR INFORMATION

Corresponding Author

*christou@chem.ufl.edu

Notes

The authors declare no competing financial interest.

■ ACKNOWLEDGMENTS

This work was supported by the NSF (G.C. DMR-1213130; S.H. DMR-1309463) and by the Air Force (S.H. AOARD 134031). T.N.N. thanks the Vietnam Education Foundation for a fellowship. Work performed at the NHMFL was supported by the National Science Foundation (DMR-1157490) and the State of Florida.

■ REFERENCES

(1) Sessoli, R.; Gatteschi, D.; Caneschi, A.; Novak, M. A. *Nature* **1993**, *365*, 141.
(2) Sessoli, R.; Tsai, H. L.; Schake, A. R.; Wang, S.; Vincent, J. B.; Folting, K.; Gatteschi, D.; Christou, G.; Hendrickson, D. N. *J. Am. Chem. Soc.* **1993**, *115*, 1804.
(3) Christou, G.; Gatteschi, D.; Hendrickson, D. N.; Sessoli, R. *MRS Bull.* **2000**, *25*, 66.
(4) Bagai, R.; Christou, G. *Chem. Soc. Rev.* **2009**, *38*, 1011.
(5) Friedman, J. R.; Sarachik, M. P.; Tejada, J.; Ziolo, R. *Phys. Rev. Lett.* **1996**, *76*, 3830.
(6) Thomas, L.; Lionti, L.; Ballou, R.; Gatteschi, D.; Sessoli, R.; Barbara, B. *Nature* **1996**, *383*, 145.
(7) Wernsdorfer, W.; Sessoli, R. *Science* **1999**, *284*, 133.
(8) Wernsdorfer, W.; Soler, M.; Christou, G.; Hendrickson, D. N. *J. Appl. Phys.* **2002**, *91*, 7164.
(9) Wernsdorfer, W.; Chakov, N. E.; Christou, G. *Phys. Rev. Lett.* **2005**, *95*, 037203.
(10) Wernsdorfer, W.; Bhaduri, S.; Tiron, R.; Hendrickson, D. N.; Christou, G. *Phys. Rev. Lett.* **2002**, *89*, 197201.
(11) Hill, S.; Edwards, R. S.; Aliaga-Alcalde, N.; Christou, G. *Science* **2003**, *302*, 1015.
(12) Wilson, A.; Hill, S.; Edwards, R. S.; Aliaga-Alcalde, N.; Christou, G. *AIP Conf. Proc.* **2006**, *850*, 1141.
(13) Tiron, R.; Wernsdorfer, W.; Foguet-Albiol, D.; Aliaga-Alcalde, N.; Christou, G. *Phys. Rev. Lett.* **2003**, *91*, 227203.
(14) Leuenberger, M. N.; Loss, D. *Nature* **2001**, *410*, 789.
(15) Zhou, B.; Tao, R.; Shen, S.-Q.; Liang, J.-Q. *Phys. Rev. A* **2002**, *66*, 010301.
(16) Affronte, M.; Troiani, F.; Ghirri, A.; Candini, A.; Evangelisti, M.; Corradini, V.; Carretta, S.; Santini, P.; Amoretti, G.; Tuna, F.; Timco, G.; Winpenny, R. E. P. *J. Phys. D: Appl. Phys.* **2007**, *40*, 2999.
(17) Vincent, R.; Klyatskaya, S.; Ruben, M.; Wernsdorfer, W.; Balestro, F. *Nature* **2012**, *488*, 357.
(18) Bogani, L.; Wernsdorfer, W. *Nat. Mater.* **2008**, *7*, 179.
(19) Katoh, K.; Isshiki, H.; Komeda, T.; Yamashita, M. *Chem. Asian. J.* **2012**, *7*, 1154.
(20) Wernsdorfer, W.; Aliaga-Alcalde, N.; Hendrickson, D. N.; Christou, G. *Nature* **2002**, *416*, 406.
(21) Nguyen, T. N.; Wernsdorfer, W.; Abboud, K. A.; Christou, G. *J. Am. Chem. Soc.* **2011**, *133*, 20688.
(22) Bagai, R.; Wernsdorfer, W.; Abboud, K. A.; Christou, G. *J. Am. Chem. Soc.* **2007**, *129*, 12918.
(23) Tiron, R.; Wernsdorfer, W.; Aliaga-Alcalde, N.; Christou, G. *Phys. Rev. B* **2003**, *68*, 140407.
(24) Yang, E.-C.; Wernsdorfer, W.; Hill, S.; Edwards, R. S.; Nakano, M.; Maccagnano, S.; Zakharov, L. N.; Rheingold, A. L.; Christou, G.; Hendrickson, D. N. *Polyhedron* **2003**, *22*, 1727.
(25) Wittick, L. M.; Murray, K. S.; Moubaraki, B.; Batten, S. R.; Spiccia, L.; Berry, K. J. *Dalton Trans.* **2004**, 1003.
(26) Miyasaka, H.; Nakata, K.; Lecren, L.; Coulon, C.; Nakazawa, Y.; Fujisaki, T.; Sugiura, K.; Yamashita, M.; Clérac, R. *J. Am. Chem. Soc.* **2006**, *128*, 3770.
(27) Inglis, R.; Jones, L. F.; Mason, K.; Collins, A.; Moggach, S. A.; Parsons, S.; Perlepes, S. P.; Wernsdorfer, W.; Brechin, E. K. *Chem.—Eur. J.* **2008**, *14*, 9117.
(28) Das, A.; Gieb, K.; Krupskaya, Y.; Demeshko, S.; Dechert, S.; Klingeler, R.; Kataev, V.; Buchner, B.; Muller, P.; Meyer, F. *J. Am. Chem. Soc.* **2011**, *133*, 3433.
(29) Jeon, I.-R.; Clérac, R. *Dalton Trans.* **2012**, *41*, 9569.
(30) Coulon, C.; Miyasaka, H.; Clérac, R. *Struct. Bonding (Berlin)* **2006**, *122*, 163−206.
(31) Xu, H.-B.; Wang, B.-W.; Pan, F.; Wang, Z.-M.; Gao, S. *Angew. Chem., Int. Ed.* **2007**, *46*, 7388.
(32) Miyasaka, H.; Yamashita, M. *Dalton Trans.* **2007**, 399−406.
(33) Bogani, L.; Vindigni, A.; Sessoli, R.; Gatteschi, D. *J. Mater. Chem.* **2008**, *18*, 4750−4758.
(34) Roubeau, O.; Clérac, R. *Eur. J. Inorg. Chem.* **2008**, 4325.

DOI: 10.1021/jacs.5b02677
J. Am. Chem. Soc. 2015, 137, 7160−7168

(35) Langley, S. K.; Chilton, N. F.; Moubaraki, B.; Murray, K. S. *Dalton Trans.* **2011**, *40*, 12201.
(36) Jones, L. F.; Prescimone, A.; Evangelisti, M.; Brechin, E. K. *Chem. Commun.* **2009**, 2023.
(37) Whitehead, G. F. S.; Moro, F.; Timco, G. A.; Wernsdorfer, W.; Teat, S. J.; Winpenny, R. E. P. *Angew. Chem., Int. Ed.* **2013**, *52*, 9932.
(38) Bellini, V.; Lorusso, G.; Candini, A.; Wernsdorfer, W.; Faust, T. B.; Timco, G. A.; Winpenny, R. E. P.; Affronte, M. *Phys. Rev. Lett.* **2011**, *106*, 227205.
(39) Bouwman, E.; Huffman, J. C.; Lobkovsky, E. B.; Christou, G.; Tsai, H.-L.; Hendrickson, D. N. A. *Inorg. Chem.* **1992**, *31*, 4436.
(40) Ung, V. A.; Thompson, A. M. W. C.; Bardwell, D. A.; Gatteschi, D.; McCleverty, J. A.; Totti, F.; Ward, M. D. *Inorg. Chem.* **1997**, *36*, 3447.
(41) Fernadez, I.; Ruiz, R.; Faus, J.; Julve, M.; Lloret, F.; Cano, J.; Ottenwaelder, X.; Journaux, Y.; Munoz, M. C. *Angew. Chem., Int. Ed.* **2001**, *40*, 3129.
(42) Pascu, M.; Lloret, F.; Avarvari, N.; Julve, M.; Andruh, M. *Inorg. Chem.* **2004**, *43*, 5189.
(43) Glaser, T.; Heidemeier, M.; Grimme, S.; Bill, E. *Inorg. Chem.* **2004**, *43*, 5192.
(44) Dul, M.-C.; Ottenwaelder, x.; Pardo, E.; Lescouezec, R.; Journaux, Y.; Chamoreau, L.-M.; Ruiz-Garcıa, R.; Cano, J.; Julve, M.; Lloret, F. *Inorg. Chem.* **2009**, *48*, 5244.
(45) Stamatatos, T. C.; Foguet-Albiol, D.; Lee, S.-C.; Stoumpos, C. C.; Raptopoulou, C. P.; Terzis, A.; Wernsdorfer, W.; Hill, S. O.; Perlepes, S. P.; Christou, G. *J. Am. Chem. Soc.* **2007**, *129*, 9484.
(46) Chakrabarty, R.; Mukherjee, P. S.; Stang, P. J. *Chem. Rev.* **2011**, *111*, 6810.
(47) Babska, A.; Bielski, L.; Kuczynski, L.; Respond, S.; Witek, H. *Pol. J. Pharmacol. Phar.* **1973**, *25*, 175.
(48) See Supporting Information.
(49) Kruger, P. E.; Moubaraki, B.; Fallon, G. D.; Murray, K. S. *J. Chem. Soc., Dalton Trans.* **2000**, 713.
(50) Mowson, A. M.; Nguyen, T. N.; Abboud, K. A.; Christou, G. *Inorg. Chem.* **2013**, *52*, 12320.
(51) Borrás-Almenar, J. J.; Clemente-Juan, J. M.; Coronado, E.; Tsukerblat, B. S. *J. Comput. Chem.* **2001**, *22*, 985.
(52) Milios, C. J.; Raptopoulou, C. P.; Terzis, A.; Lloret, F.; Vicente, R.; Perlepes, S. P.; Escuer, A. *Angew. Chem., Int. Ed.* **2004**, *43*, 210.
(53) Milios, C. J.; Vinslava, A.; Wernsdorfer, W.; Moggach, S.; Parsons, S.; Perlepes, S. P.; Christou, G.; Brechin, E. K. *J. Am. Chem. Soc.* **2007**, *129*, 2754.
(54) Martínez-Lillo, J.; Tomsa, A. R.; Li, Y.; Chamoreau, L.-M.; Cremades, E.; Ruiz, E.; Barra, A.-R.; Proust, A.; Verdaguer, M.; Gouzerh, P. *Dalton Trans.* **2012**, *41*, 13668.
(55) Martínez-Lillo, J.; Dolan, N.; Brechin, E. K. *Dalton Trans.* **2014**, *43*, 4408.
(56) Poole, K. M.; Korabik, M.; Shiddiq, M.; Mitchell, K. J.; Fournet, A.; You, Z.; Christou, G.; Hill, S.; Holynska, M. *Inorg. Chem.* **2015**, *4*, 1883.
(57) Liu, J.; del Barco, E.; Hill, S. A Microscopic and Spectroscopic View of Quantum Tunneling of the Magnetization. In *Molecular Magnets—Physics and Applications*; Bartolomé, J., Luis, F., Fernández, J. F., Eds.; Springer-Verlag: Berlin-Heidelberg, 2014; pp 77—110.
(58) Liu, J.; del Barco, E.; Hill, S. *Phys. Rev. B* **2012**, *85*, 012406.
(59) Stoll, S.; Schweiger, A. *J. Magn. Reson.* **2006**, *178*, 42.
(60) Hill, S.; Wilson, A. *J. Low Temp. Phys.* **2006**, *142*, 267.
(61) Feng, P. L.; Koo, C.; Henderson, J.; Manning, P.; Nakano, M.; del Barco, E.; Hill, S.; Hendrickson, D. N. *Inorg. Chem.* **2009**, *48*, 3480.
(62) Hill, S.; Datta, S.; Liu, J.; Inglis, R.; Milios, C. J.; Feng, P. L.; Henderson, J. J.; del Barco, E.; Brechin, E. K.; Hendrickson, D. N. *Dalton Trans.* **2010**, *39*, 4693.
(63) Inglis, R.; Jones, L. F.; Milios, C. J.; Datta, S.; Collins, A.; Parsons, S.; Wernsdorfer, W.; Hill, S.; Perlepes, S. P.; Piligkos, S.; Brechin, E. K. *Dalton Trans.* **2009**, *38*, 3403.
(64) Houton, E.; Taylor, S. M.; Beedle, C. C.; Cano, J.; Piligkos, S.; Hill, S.; Ryder, A. G.; Brechin, E. K.; Jones, L. F. *Dalton Trans.* **2012**, *41*, 8340.
(65) Chen, S.-Y.; Beedle, C. C.; Gan, P.-R.; Lee, G.-H.; Hill, S.; Yang, E.-C. *Inorg. Chem.* **2012**, *51*, 4448.
(66) Hill, S.; Murugesu, M.; Christou, G. *Phys. Rev. B* **2009**, *80*, 174416.
(67) *SHELXTL6*; Bruker-AXS: Madison, WI, 2008.
(68) van der Sluis, P.; Spek, A. L. *Acta Crystallogr.* **1990**, *A46*, 194.
(69) Spek, A. L. *Acta Crystallogr.* **1990**, *A46*, C34.
(70) Takahashi, S.; Hill, S. *Rev. Sci. Instrum.* **2005**, *76*, 023114.
(71) Mola, M.; Hill, S.; Goy, P.; Gross, M. *Rev. Sci. Instrum.* **2000**, *71*, 186.
(72) Hassan, A. K.; Pardi, L. A.; Krzystek, J.; Sienkiewicz, A.; Goy, P.; Rohrer, M.; Brunel, L. C. *J. Magn. Reson.* **2000**, *142*, 300.
(73) Davidson, E. R. *MAGNET*; Indiana University: Bloomington, IN, 1999.

DOI: 10.1021/jacs.5b02677
J. Am. Chem. Soc. 2015, 137, 7160—7168